Liquid-Phase Sintered SiC Ceramics with Oxynitride Additives

G. Rixecker, K. Biswas, I. Wiedmann and F. Aldinger

Max-Planck Institut für Metallforschung and
Institut für Nichtmetallische Anorganische Materialien der Universität Stuttgart,
Pulvermetallurgisches Laboratorium, Stuttgart, Germany

Abstract

Silicon carbide ceramics with sintering additives from the system AlN-Y_2O_3 can be gas-pressure sintered to theoretical density. While commonly a combination of sesquioxides is used such as Al_2O_3-Y_2O_3, the oxynitride additives offer the advantage that only a nitrogen atmosphere is required instead of a powder bed for thermochemical stabilisation at the sintering temperature. When a moderate nitrogen overpressure is applied, mass loss during densification becomes small and depends only on the oxygen content of the SiC starting powder. By starting from a mixture of β-SiC and α-SiC, and by performing dedicated heat treatments after densification, anisotropic grain growth is obtained which leads to a platelet microstructure showing enhanced fracture toughness. In the present work, recent improvement of the mechanical behaviour of these materials at ambient and high temperatures is reported. By means of a surface oxidation treatment in air it is possible to obtain four-point bending strengths in excess of 1 GPa, and the strength retention at high temperatures is significantly improved.

1. Introduction

Silicon carbide is an important structural material because of its unique combination of properties, such as high temperature strength, resistance to wear and corrosion, and thermal shock resistance. In the early 1980s [1], liquid phase sintering (LPS) was recognised as an innovative approach to the densification of SiC, allowing ceramics with a controlled, fine-grained microstructure—and consequently improved reliability—to be obtained. Following the customary densification route of silicon nitride ceramics, Al_2O_3-Y_2O_3 was used as a sintering additive [2-4]. In this way, and by using the anisotropic grain growth exhibited by α-SiC, superior self-reinforced SiC was successfully fabricated [5,6].

Lee and Wei [7] found AlN additions to be beneficial in the liquid phase sintering of SiC with yttria and/ or alumina additives. The sinterability of SiC using a combination of AlN and Y_2O_3 was first described by *Chia et al.* [8] and by *Nader* [9]. In contrast to the 'conventional' additive system, Al_2O_3-Y_2O_3, silicon carbide can be densified reproducibly without a powder bed by using AlN-Y_2O_3 as the sintering aid. This is because the decomposition reaction

$$2\,AlN \longrightarrow 2\,Al_{(l)} + N_{2(g)}$$

is suppressed quite effectively by applying a nitrogen overpressure; in contrast, the partial reduction of alumina at sintering temperatures [3,9],

$$Al_2O_3 + SiC \longrightarrow Al_2O_{(g)} + SiO_{(g)} + CO_{(g)},$$

is much more difficult to control. Yttria does not show appreciable gas phase reactions with SiC at temperatures below 2000 °C [9,10].

The microstructure of LPS-SiC materials can be controlled by varying the ratio of α-SiC to β-SiC in the starting powder and by applying suitable post-sintering heat treatments. It was shown [9,11] that, in case of compacts derived from α-SiC powder, the aspect ratio of the SiC grains changes only slightly during post-sintering heat treatments. With β-SiC starting

powders, the aspect ratio can be significantly increased by anisotropic grain growth resulting in a microstructure with interlocking plate-like grains. Since the formation of this 'in-situ platelet-strengthened' microstructure depends on the occurrence of the phase transformation of β-SiC to α-SiC (the grain growth anisotropy is a feature of the hexagonal crystal symmetry of α-SiC), it can be largely accelerated by adding some α-SiC as transformation seeds [12-15]. The fracture toughness of LPS-SiC, which depends rather sensitively on the aspect ratio, is enhanced as fracture energy-dissipating mechanisms, like crack bridging and crack deflection, become operational in the platelet microstructure [16,17].

2. Experimental

The starting materials for this study were purchased from H. C. Starck, Germany, and characterised for particle size distribution (laser granulometry) and specific surface area (N_2 adsorption isotherms, BET). Chemical analyses of the powders were provided by the manufacturer: α-SiC A-10, d_{50} = 0.51 μm, 11.1 m^2/g, 0.9 wt % O; β-SiC BF-12, d_{50} = 0.89 μm, 17.8 m^2/g, 1.2 wt % O; AlN Grade C, d_{50} = 0.92 μm, 5.0 m^2/g, 2.5 wt % O; and Y_2O_3 Grade C, d_{50} = 4.48 μm, 12.0 m^2/g. Compositional variations of the powder mixtures prepared include the ratio of β-SiC to α-SiC (100, 96, 90, 0 % β-SiC), the molar ratio of AlN to Y_2O_3 in the sintering additive (80, 60, 40, 20 % AlN), and the amount of additive (10 or 7 vol %). The nomenclature of "mol % of β-SiC in SiC – mol % of AlN in additive (– vol % additive content)" is also used to describe the samples after sintering, irrespective of changes in the phase composition. The powder mixtures were prepared by attrition milling for 4 h in isopropanol, using Si_3N_4 milling media and polyamide containers and stirrers. The slurry was separated from the milling media and possible wear debris by screening and pre-dried in a rotating evaporator. Completely dried powders were obtained after 24 h in a drying oven at 64 °C. They were subsequently sieved to obtain granules with a maximum size of 160 μm. Green body compaction was done by cold isostatic pressing at 240 MPa.

Sintering and post-sintering heat treatments were conducted in gas pressure furnaces with graphite heating elements under nitrogen pressures between 0.1 MPa and 10 MPa. Sintering temperatures up to 2050 °C were used. Containerless post-HIP at 2000 °C/ 200 MPa N_2 was applied to compositions that could be gas-pressure sintered to closed porosity but not to theoretical density. The specimens were kept in covered boron nitride crucibles for sintering and heat treatments in order to neutralise the reducing furnace atmosphere. The mass loss during sintering was measured for all sintered samples by weighing the green and sintered bodies. Additional thermogravimetric (TGA) experiments were performed using a thermobalance. Sintered densities were measured using Archimedes' method in water. The theoretical density was calculated from the densities of the starting phases by the rule of mixtures. Relative densities in excess of 100 % are attributed to the fact that the phase transformations during sintering are neglected in the calculation.

X-ray powder diffractometry was performed using monochromatised CuK_α radiation and a position sensitive detector with a collection angle of 8°. For quantitative phase analysis by XRD, the sintered bodies were pulverised to exclude texture effects. Single peak fitting with Pseudo-Voigtian line profiles was used to deconvolute relative line intensities. Specimen preparation to reveal the grain boundary phase in scanning electron microscopy images included a final polishing step with 1 μm diamond suspension and a subsequent plasma etching treatment in an equimolar mixture of CF_4 and O_2. Microstructures were examined by scanning electron microscopy, using either a conventional SEM (S 200, Cambridge Instruments, GB) or a microscope featuring thermal Schottky field emission cathode and a dedicated column design for high resolution at low acceleration voltages (DSM 982, Zeiss, Germany). Both instruments include energy-dispersive microprobe analysis (EDX). While the electron energies of 3 to 4 keV which are accessible with the Zeiss microscope allow LPS-SiC to be imaged without any specimen coating, carbon coating had to be used at the 'standard' acceleration voltage of 15 kV in order to avoid charging effects.

Fracture toughness was determined by using the indentation method. After polishing to a 1 μm finish, 12 Vickers indentations per specimen were introduced with a load of 50 N. A formula valid for semi-circular crack systems [18] was used to calculate K_{Ic} from the lengths of edge cracks and indentation diagonals. Young's moduli were measured by the pulse-echo method, and a value of 400 (± 20) MPa was used for K_{Ic} determination. For the strength measurements, four-point bending fixtures with inner and outer spans of 20 and 40 mm were used. Samples with dimensions of 3 × 4 × 48 mm^3 were cut from larger sintered bars by means of a diamond saw. After grinding on all sides, the tensile surfaces were polished to a 3 μm finish and the tensile edges were bevelled to remove stress concentrations and edge flaws caused by sectioning. Room temperature testing was accomplished with an hydraulic testing machine at a constant cross head displacement rate of 5 mm/s. For each material, at least 6 specimens were tested. High temperature testing was performed in air, at temperatures between 1000 °C and 1500 °C, using a universal testing machine. A dwell time of 10 min at the testing temperature was allowed to ensure temperature homogeneity. The samples were loaded with a cross head speed of 0.1 mm/min. In most cases, only one or two specimens were tested at each temperature, i. e. the high-temperature strength data have a preliminary character.

3. Sintering Behaviour

Figure 1 depicts the sintering cycle used for gas-pressure sintering. Heating rates of 20 °C/min from ambient temperature to 1600 °C and 10 °C/min from 1600 °C to the final sintering temperature were used. The holding time of 30 min at 1600 °C was devised to allow for the thermal decomposition of SiO_2 from the surface of the SiC starting powders (≈ 2.4 wt % of oxygen, according to manufacturer's analysis) [9]:

$$2\ SiO_2 + SiC \longrightarrow 3\ SiO_{(g)} + CO_{(g)}.$$

According to the TGA scan of Figure 2, which was recorded in flowing nitrogen atmosphere, this reaction starts at about 1500 °C. The further weight loss above 1700 °C is due to the thermal decomposition of AlN.

Figures 1, 2.

For isothermal densification, a two-stage sintering scheme with two holding times of 30 min and a base nitrogen pressure of 0.1 or 0.2 MPa was adopted. The second stage was performed either under the same pressure or under 10 MPa N_2. In order to find the proper sintering temperature, the temperature of successive runs (30 min, 0.2 MPa N_2), was increased in steps of 30 K until a relative density in excess of 98 % was reached. Upon joining the second sintering stage, this led to final densities ≥ 99.4 % . In ceramics derived from β-SiC powders, an annealing stage after densification is added for the in-situ conversion of equiaxed β-SiC grains into α-SiC platelets (see section 4). These post-sintering heat treatments were conducted at 1950 °C/ 0.2 MPa N_2, with heating rates restricted to 10 K/min to minimise thermal stresses.

As shown in Fig. 3, the sintering temperature for complete densification ($\rho \geq 99.5$ %) is a function of the additive composition. Interestingly, however, the best densification behaviour does not coincide with the eutectic composition in the AlN-Y_2O_3 system, which is at 40 mol % AlN [19]. Comparing different N_2 pressures (0.1, 0.2, and 10 MPa), there is a tendency for the sintering temperature to be particularly low at an intermediate pressure. For the materials 100α-80AlN and 100α-40AlN, dense samples were obtained by pressureless sintering as well. However, the densification temperature of the more N_2-rich composition is significantly higher at 0.1 MPa N_2, which is indicative of the concurrent dissociation of AlN. With a base pressure of 0.2 MPa, and 10 MPa N_2 being applied during the second half of the sintering time, the total weight loss is restricted to about 2.5 %, roughly corresponding to the oxygen content of the SiO_2 layer on the surface of the starting powder [9,20]. On the other hand, sintering at 10 MPa requires higher densification temperatures at intermediate nitrogen contents of the additive. It is well known that the

viscosity of silicate melts increases with their nitrogen content, in analogy to the enhanced glass transition temperatures of oxynitride glasses [21-22]. Thus, there is a competition between the thermochemical stabilisation of AlN and the obstruction of atomic transport by the increased melt viscosity.

Figure 3.

Table 1 gives an overview of some pressure sintering runs that were optimised for larger bar-shaped samples of about 12 × 20 × 50 mm^3. At the smallest nitrogen content (90β-20AlN), it was not possible to achieve full densification by gas pressure sintering. Therefore, this material was post-HIPed at 2000 °C/ 200 MPa N_2. The sluggish densification is not due to a lack of liquid phase at the sintering temperature, but rather due to its poor wetting, as can be inferred from SEM micrographs.

Table 1.

4. Phase composition, microstructure, and fracture toughness

The starting powders used in this study contain exclusively the silicon carbide polytypes 6H (α-SiC) and 3C (β-SiC). By XRD, these polytypes were found to be predominant in as-sintered samples as well, with trace amounts of 4H, 15R and 33R being present in materials derived from pure α-SiC (Table 2). During subsequent heat treatments at 1950 °C, minor admixtures of 4H, 15R and 33R also appeared in compositions based on β-SiC. For an estimate of the ratio of β-SiC to α-SiC, however, only the relative intensities of the Bragg reflections $(101)_{6H}$ and $[(006)_{6H}+(111)_{3C}]$ were taken into account. They were evaluated by comparison with a calibration curve [20] obtained from appropriate mixtures of α-SiC (Lonza, Germany) and β-SiC (Ibiden, Japan) powders that were selected for their phase purity. The kinetics of the β → α transition are shown in Fig. 4 for a range of different compositions. A maximum in the transformation rate was observed for the 90β-60AlN material, where the transformation was almost completed after 6 h at 1950 °C. Changes in the chemical composition as well as decreased additive or α-SiC contents reduced the

rapidity of the phase transformation. In the extreme case of 100β-60AlN, which has the same chemical composition as 90β-60AlN but no α-SiC seeds, only 54 % α-SiC was present after 20 h of annealing[1].

Table 2.

Figure 4.

In the present LPS-SiC materials, the intergranular phase is partly crystalline after sintering. The crystallisation, which is thought to occur at multigrain junctions, leads to a variety of oxide and oxynitride phases. Qualitative analysis of the secondary phases by XRD was done by comparison with JCPDS standards [23]. In addition to the phases indicated in Table 2, traces of $Y_2Si_2O_7$, $Y_4Al_2O_9$, $Y_3Al_5O_{12}$ and a cubic phase similar to YN were found. With the exception of the additive-lean composition 90β-60AlN-7Add, the oxynitride phases are converted to oxides during 16 h at 1950 °C, although all heat treatments were performed in 0.2 MPa N_2 atmosphere. For the composition 90β-60AlN, the total weight loss during densification and the subsequent heat treatment was 7 %.

Figure 5 shows a fine-grained equiaxed microstructure as it is formed in LPS-SiC ceramics derived from pure α-SiC powder. The intergranular phase forms a continuous grain boundary film with a thickness on the order of 1 nm [25]. Depending on the plasma etching conditions, these grain boundary films are usually visible in SEM images at magnifications around 10^4, because they are etched to a much lesser extent than the SiC matrix and form protruding ridges.

Figure 5.

During liquid phase sintering, dissolution of SiC in the melt takes place. In heavily etched samples (Fig. 5), the re-precipitation of material on the undissolved 'cores' of the α-SiC grains is obvious [9,20,24]. The 'rim' regions are seen by EDX to be strongly doped with

[1] In order to nucleate the β → α transformation, the grain size distribution of 100β-60 AlN was artificially made bimodal by adding 10 % of a coarser β-SiC powder (H. C. Starck B-hp) [6].

Al, and are therefore more resistant against the fluorine plasma than the more chemically clean SiC in the core regions. Relatively little grain growth occurs during densification, indicating that either the interfacial reactions involved or the atomic transport through the melt may be sluggish. As it has already been mentioned, the viscosity of oxynitride glasses increases with increasing nitrogen content. However, the rate of grain growth during sintering of the present LPS-SiC materials is found to increase with increasing AlN content of the sintering additive (Fig. 6), providing a clear indication that the grain growth is not controlled by the atomic transport but rather by interfacial reactions. The same conclusion has been arrived at by proving grain growth to be independent of the additive content [26]. It was also shown, that the corrosive attack on SiC single crystals by oxynitride melts similar to the AlN-Y_2O_3 additives used in this study is extremely slow [27]. It is thus likely that the dissolution reaction is the rate limiting step for grain growth. To verify this directly, the amount of intergranular phase must be shown to stay constant during isothermal heat treatments; this is the case, e. g., in the system Si_3N_4-SiO_2-Y_2O_3 [28].

Figure 6.

In samples that are rich in β-SiC, the solution/ precipitation process is accompanied by the β-SiC → α-SiC phase transformation, as discussed above. The newly formed α-SiC crystallites exhibit anisotropic grain growth, the preferred growth direction being perpendicular to the stacking planes of SiC_4 tetrahedra. In analogy to the rod-like grains of β-Si_3N_4 [29], the crystallites continue to grow to a platelet-like morphology until there is steric hindrance by the neighbouring grains [9]. The fracture mode of the present LPS-SiC is mostly intergranular, the additive phase being mechanically weaker than silicon carbide [9,30]. In the fine-grained globular microstructure of 100α-60AlN (Fig. 5), the indentation fracture toughness has a value of K_{Ic}= 4.4 ± 0.2 MPa$\sqrt{m}$. In platelet microstructures, it increases significantly as the dissipation of fracture energy by crack wake interactions (crack deflection, branching, elastic bridging and mechanical interlocking) becomes effective [16,17].

Figure 7 shows the microstructures of (a) 90β-40AlN and (b) 96β-60AlN after an annealing time of 24 h at 1950 °C. In both cases, the $\beta \rightarrow \alpha$ transformation is completed, and the K_{Ic} values have reached the plateau values of 4.9 ± 0.5 MPa$\sqrt{m}$ and 6.0 ± 0.5 MPa$\sqrt{m}$, respectively (Fig. 8). In two-dimensional sections through a platelet microstructure, very few grains are viewed both edge-on and close to their largest diameter. While a stringent treatment deriving microstructural parameters from 2-D sections of prismatic plates [31], is beyond the scope of this work, a rough estimate is possible by assuming the highest elongations that occur in the micrographs to be representative of the average aspect ratio r_a of the 3-D grains. If the top 4 % of elongations in the two images of Fig. 7 are taken into account, r_a is obtained as 3.3 and 3.9, respectively, confirming the positive correlation between r_a and K_{Ic}. Upon completion of the $\beta \rightarrow \alpha$ transition, however, the steric hindrance between neighbouring platelets restricts anisotropic grain growth whereas the general coarsening of the microstructure is going on. Therefore, r_a decreases again in over-annealed samples, e. g. from 3.7 (after 10 h at 1950 °C) to 3.4 (16 h at 1950 °C) in 90β-60AlN. As the fracture toughness tends to increase with increasing grain size [32], materials with a relatively fast transformation kinetics show a maximum in K_{Ic} whereas those with a more sluggish transformation approach a plateau value (Fig. 8).

Figures 7, 8.

For the 90β materials, the as-sintered fracture toughness is highest at the additive composition 60AlN, corresponding to the fastest $\alpha \rightarrow \beta$ transformation (Fig. 4). The SEM image Fig. 6(b) illustrates that 90β-60AlN has elongated grains already in the as-sintered state; a maximum of K_{Ic} = 5.9 ± 0.5 MPa$\sqrt{m}$ is obtained after 10 h of annealing. Among the 60AlN materials, K_{Ic} in the annealed state depends on the initial volume fraction of α-SiC: the larger the spacing of the seeds, the longer time is available for anisotropic grain growth until the platelets impinge. In 96β-60AlN samples, K_{Ic}= 6.5 ± 0.5 MPa$\sqrt{m}$ was measured after 32 h of annealing. Even after this time, 100β-60AlN with its extremely sluggish transformation behaviour reached only K_{Ic}= 5.0 ± 0.4 MPa$\sqrt{m}$ (Fig. 9).

Figure 9.

5. Mechanical Strength

Figure 10 summarises the room temperature bending strength measurements. Among the materials 90β-40AlN, 90β-60AlN and 90β-80AlN, there is no obvious dependence of the room temperature strength on either the chemical composition of the sintering additive or the grain size – cf. Fig. 6. Furthermore, a comparison between 90β-60AlN in the as-sintered condition and after a heat treatment for 7 h at 1950 °C shows, that the still fine-grained and homogeneous microstructure obtained by annealing does not affect the strength adversely. In contrast, the volume fraction of mechanically weak intergranular phase at multigrain junctions does have an influence on the strength behaviour [30]. Accordingly, reducing the additive content to 7 vol % yields a somewhat increased bending strength of 526 ± 95 MPa, indicating that the present materials have some potential for improving σ^{4pt}_{RT} while retaining good sinterability. Although the dependence of σ^{4pt}_{RT} on grain size and shape is weak within the 90β series, the more fine-grained (≤ 2 μm) and equiaxed material 100α-60AlN (Fig. 5) also shows a higher strength level of 564 ± 15 MPa [16].

Selected results from high temperature strength measurements are plotted in Fig. 11. With either 40 % AlN in the additive, or a smaller additive content of 7 vol %, the good strength retention up to 1200 °C is followed by a sharp decrease at 1400 °C. This is a common temperature limit for monolithic ceramics with silicon-rich glassy phases at the grain boundaries. For ceramics with the additive composition 60 AlN and the larger additive content of 10 vol %, however, strength retention is excellent until 1400°C. At that temperature, σ^{4pt} of the material 90β-60AlN effectively takes on a peak value of 551 MPa, followed by a drop to 419 MPa at 1500°C. The occurrence of this strength maximum can be explained by the generation of large compressive stresses due to selective oxidation of the oxynitridic intergranular phases to oxides ($Y_3Al_5O_{12}$, $Y_2Si_2O_7$) having a lower density than

the oxynitrides [11]. Analogous observations have also been reported for other non-oxide ceramics, such as Si_3N_4 [33] and Al_2O_3-SiC [34].

Figure 11.

In an attempt to conserve the enhanced high-temperature strength at room temperature, samples having the nitrogen-rich composition 100α-80AlN were oxidised by isothermal heat treatments at 1200°C in air. The resulting room temperature strengths are markedly higher than those of unoxidised samples, e. g. $\sigma^{4pt} = 1047 \pm 202$ MPa after an annealing time of 12 min (Fig. 12). Upon continued oxidation, σ^{4pt} decreases again, but the residual strength after 6000 min is still higher than the starting value. As a further evidence for the proposed mechanism, measurements of indentation fracture toughness reveal a distinct increase of the apparent K_{Ic}, from 4.0 ± 0.4 MPa$\sqrt{m}$ in as-sintered specimens to 5.6 ± 0.3 MPa after 12 min at 1200°C [35]. Since the layer thickness tested by the Vickers indentations is about 50 μm, the stress state can be estimated to extend ≥ 10 μm into the material. The Weibull modulus, which can be extracted from a plot of failure probability against bending stress, increases from m = 7 to m = 13 and indicates an enhanced reliability of the ceramics. In other words, the ambient strength of the present materials is largely determined by surface flaws, whereas the bulk microstructure is sufficiently defect-free to allow a strength level of about 1 GPa to be achieved.

Figure 12.

6. Conclusions

- Fully dense SiC ceramics were obtained by liquid phase sintering with AlN-Y_2O_3 additives. While pressureless sintering in nitrogen atmosphere is effective for the complete densification of a wide range of compositions, sintering in a N_2 overpressure of 0.2 to 10 MPa proved advantageous in view of microstructural control.
- The materials obtained are fine-grained and homogeneous and have a good potential for microstructure design by the in-situ growth of α-SiC platelets. The phase transformation

from β-SiC to α-SiC, the anisotropic grain growth, and the evolution of high fracture toughness are all strongly correlated. Materials with 60 mol % AlN in the sintering additive exhibit the fastest kinetics. The maximum in fracture toughness depends on the amount of α-SiC seeds added to the starting powders. At a reduced α-SiC content of 4 %, K_{Ic}= 6.5 ± 0.5 MPa$\sqrt{m}$ was measured.

• High temperature strength is characterised by the occurrence of a maximum around 1200 °C. Again, the most favourable strength behaviour up to 1400 °C is obtained with the 60 vol % AlN composition. The reason for the strengthening effect at high temperatures, which is characteristic of the additive system AlN-Y_2O_3, is believed to be the generation of compressive stress by oxidation of intergranular oxynitride phases. Thus, the strength curve is the result of a concurrence between softening of the intergranular phase in the bulk and oxidation-induced surface strengthening.

• Room temperature bending strengths are higher (~ 550 MPa) for more fine-grained and equiaxed microstructures, indicating that a tradeoff between strength and fracture toughness has to be accepted. On the other hand, there seems to be scope for improving the strength by decreasing the amount of sintering additives below 7 vol % while retaining good sinterability.

• A bending strength of about 1 GPa at room temperature can be obtained by a rather uncritical heat treatment in air of the nitrogen-rich composition 100α-80AlN. The magnitude of the effect and the significant thickness of the influenced layer create a potential for application in enhancing the reliability of LPS-SiC parts.

Acknowledgements

K. B. gratefully acknowledges a scholarship within the DAAD/ IIT sandwich programme. The authors are thankful to the technical staff of PML Stuttgart for assisting with the experimental work.

References

[1] M. Omori and H. Takei, J. Am. Ceram. Soc. 65 (1982) C-92.

[2] N. P. Padture and B. R. Lawn, J. Am. Ceram. Soc., 77 (1992) 2518.

[3] M. A. Mulla and V. D. Kristic, J. Mater. Sci. 29 (1994) 934.

[4] M. A. Mulla and V. D. Kristic, Acta. Metall. 42 (1994) 303.

[5] N. P. Padture, J. Am. Ceram. Soc. 77 (1994) 519.

[6] Y. W. Kim, M. Mitomo and H. Hirotsuru, J. Am. Ceram. Soc. 78 (1995) 3145; J. Am. Ceram. Soc. 80 (1997) 99.

[7] R. R. Lee and W. C. Wei, Ceram. Engng. Sci. Proc. 11 (1990) 1094.

[8] K. Y. Chia, W. D. G. Böcker and R. S. Storm, U. S. Pat. 5,298,470 (1994).

[9] M. Nader, Doctoral Thesis, Univ. of Stuttgart, 1995.

[10] H. J. Seifert, H. L. Lukas and F. Aldinger, in: Design Fundamentals of High Temp. Compos., Intermetallics, and Metal-Ceramics Systems, R. Y. Lin et al. (eds.), The Minerals, Metals & Mater. Soc., Warrendale, 1995, p. 297 ff.

[11] G. Rixecker, I. Wiedmann and F. Aldinger, cfi. – Ber. Dt. Keram. Ges. Beihefte 15/1 (2000) 147-156.

[12] S. K. Lee and C. H. Kim, J. Am. Ceram. Soc. 77 (1994) 1655.

[13] H. Kodama and T. Miyoshi, J. Am. Ceram. Soc. 75 (1992) 1558.

[14] Y. W. Kim, M. Mitomo, H. Emoto and J. G. Lee, J. Am. Ceram. Soc. 81 (1998) 3136.

[15] K. Biswas, M. Tech. Thesis, Ind. Inst. Technol. Kanpur and Univ. of Stuttgart, 1999.

[16] M. Keppeler, H. G. Reichert, J. M. Broadley, G. Thurn, I. Wiedmann and F. Aldinger, J. Eur. Ceram. Soc. 18 (1998) 521.

[17] P. F. Becher, J. Am. Ceram. Soc. 74 (1991) 255.

[18] G. R. P. Anstis, P. Chantikul, B. R. Lawn and D. B. Marshall, J. Am. Ceram. Soc. 64 (1981) 533.

[19] A. Jeutter, Diplom Thesis, Univ. of Stuttgart, 1993.

[20] I. Wiedmann, Doctoral Thesis, Univ. of Stuttgart, 1998.

[21] R. A. L. Drew, S. Hampshire and K. H. Jack, in: Progress in Nitrogen Ceramics, F. L. Riley (ed.), Martinus Nijhoff Publ., Boston, 1983, p. 323 ff.

[22] S. Hampshire, E. Nestor, R. Flynn, J.-L. Besson, T. Rouxel, H. Lemercier, P. Goursat, M. Sebai, D. P. Thompson and K. Liddell, J. Eur. Ceram. Soc. 14 (1994) 261.

[23] Joint Committee on Powder Diffraction Standards, ASTM, Swartmore, 1995.

[24] L. S. Sigl and H.-J. Kleebe, J. Am. Ceram. Soc. 76 (1993) 773.

[25] L. K. L. Falk, J. Eur. Ceram. Soc. 17 (1997) 983.

[26] H. Ye, V. V. Pujar and N. P. Padture, Acta mater. 47 (1999) 481.

[27] T. Eschner and F. Aldinger, unpublished work (1999).

[28] S. Ordoñez, I. Iturriza and F. Casatro, J. Mater. Sci. 34 (1999) 147.

[29] M. Krämer, M. J. Hoffmann and G. Petzow, Acta metall. mater. 41 (1993) 2939.

[30] M. J. Hoffmann and M. Nader, in: Engn. Ceram. '96: Higher Reliability through Proces., G. N. Babini et al. (eds.), Kluwer Acad. Publ., Dordrecht, 1997, p. 133 ff.

[31] F. Mücklich, J. Ohser, S. Blank, D. Katrakova and G. Petzow, Z. Metallkd., 90 (1999) 8.

[32] H.-J. Kleebe, G. Pezzotti and G. Ziegler, J. Am. Ceram. Soc. 82 (1999) 1857.

[33] S. R. Choi and V. Tikare, Scr. Metall. 26 (1992) 1263.

[34] I. A. Chou, H. M. Chan and P. Harmer, J. Am. Ceram. Soc. 81 (1998) 1203.

[35] M. F. Gruninger, B. R. Lawn, E. N. Farabough and J. B. Wachtman, J. Am. Ceram. Soc. 70 (1987) 344.

Tables

Table 1: Sintered density and mass loss data

Sample	Sintering Temp. [°C]	Max. N_2 pressure [MPa]	Mass loss [%]	ρ_{theor} [g/cm^3]	ρ_{rel} [%]
90β-20AlN	2010-2030	10	1.4-2.0	3.36	94.9-96.4
90β-20AlN (post-HIP)	2000	200	–0.4	3.36	99.4
90β-40AlN	1980	10	2.3-2.4	3.34	99.6-100.0
90β-60AlN	2010	10	2.4-2.6	3.32	100.2
96β-60AlN	1980	10	2.5	3.32	100.2-100.3
90β-60AlN-7Add	2020	10	3.0-3.1	3.28	100.1-100.4
100α-60AlN	1950	10	1.9	3.32	100.5-100.7
100α-80AlN	2000	10	2.2-2.3	3.28	100.5
100β-60AlN	1980	10	2.4-2.5	3.32	100.2-100.5

Table 2: Phase analysis data as a function of annealing time

Crystalline phases	100α-60AlN as-sintered	90β-60AlN as-sintered	90β-60AlN ann. 1950 °C/ 16 h
major:	α-SiC (6H)	β-SiC (3C) α-SiC (6H)	α-SiC (6H)
minor:			
α-SiC (4H, 15R, 33R)	■		■
$Y_{10}Al_2Si_3O_{18}N_4$	■	■	■
$Y_4Si_2O_7N_2$		■	
Y_2SiO_5			■
Y_2O_3	■	■	■

Figure Captions

Figure 1. Liquid phase/ gas pressure sintering cycles for α-SiC and β/α-SiC; post-densification heat treatments for the microstructure design of β/α-SiC

Figure 2. Thermogravimetric analysis of 90β-60AlN powder in flowing nitrogen atmosphere; heating rates of 25 K/min ($T \leq 1500$ °C) and 10 K/min ($T > 1500$°C)

Figure 3. Sintering behaviour as a function of N_2 pressure and nitrogen content in the additive; sintering temperatures for a final density ≥ 99.5 %

Figure 5. Fine grained-globular microstructure of 100α-60AlN, heavily plasma-etched to reveal grain boundary phases and core/ rim structure of α-SiC grains

Figure 4. Kinetics of the phase transformation β-SiC (3C) → α-SiC (6H)

Figure 6. Microstructure of as-sintered materials: (a) 90β-40AlN, (b) 90β-60AlN, (c) 90β-80AlN

Figure 7. Platelet microstructures obtained after annealing (1950 °C/ 24 h): (a) 90β-40AlN, (b) 96β-60AlN

Figure 8. Development of fracture toughness as a function of the annealing time at 1950 °C

Figure 9. Maximum fracture toughness as a function of the seed density/ corresponding annealing times at 1950 °C
(data at 20 % α-SiC: from [9], annealed at 1925 °C)

Figure 10. Four-point bending strengths at ambient temperature

Figure 11. High-temperature bending strength of some β-SiC based compositions

Figure 12. Strength and apparent fracture toughness as a function of the oxidation time at 1200 °C

Figure 1.

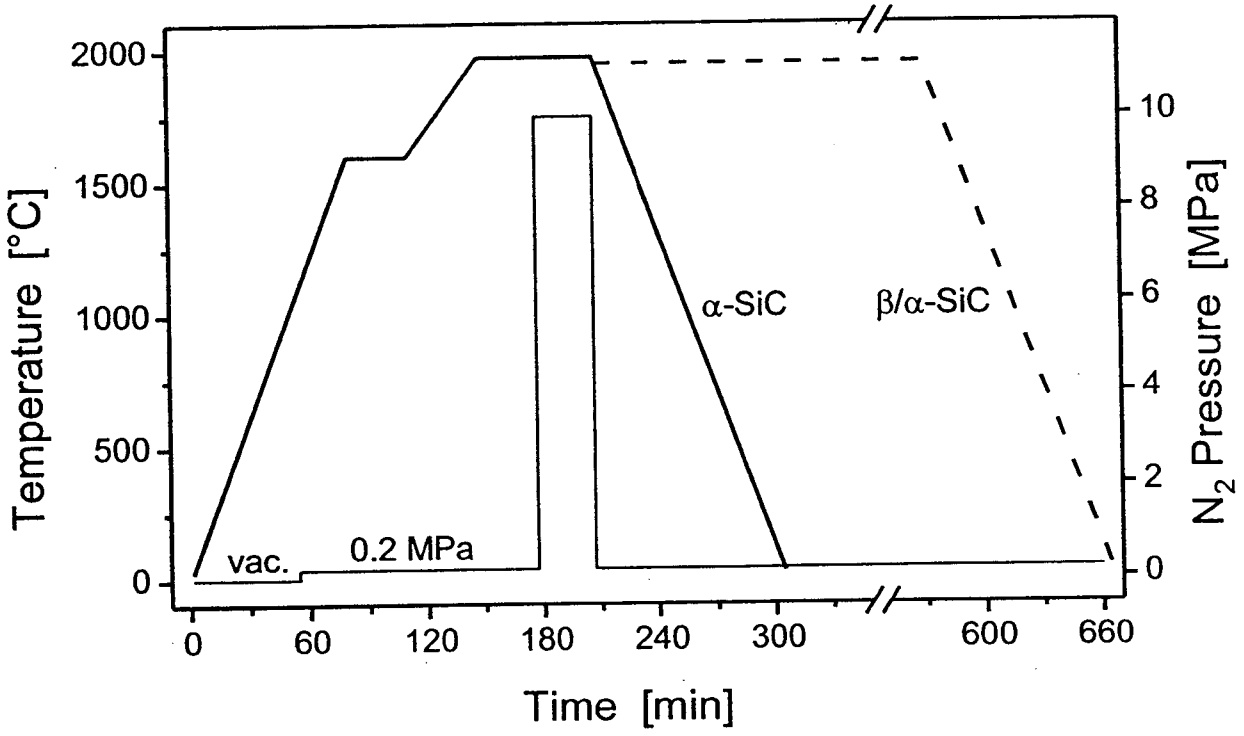
Temperature [°C]
2000
1500
1000
500
0
vac.
0.2 MPa
α-SiC
β/α-SiC
0
60
120
180
240
300
600
660
Time [min]
N2 Pressure [MPa]
10
8
6
4
2
0

Figure 2.

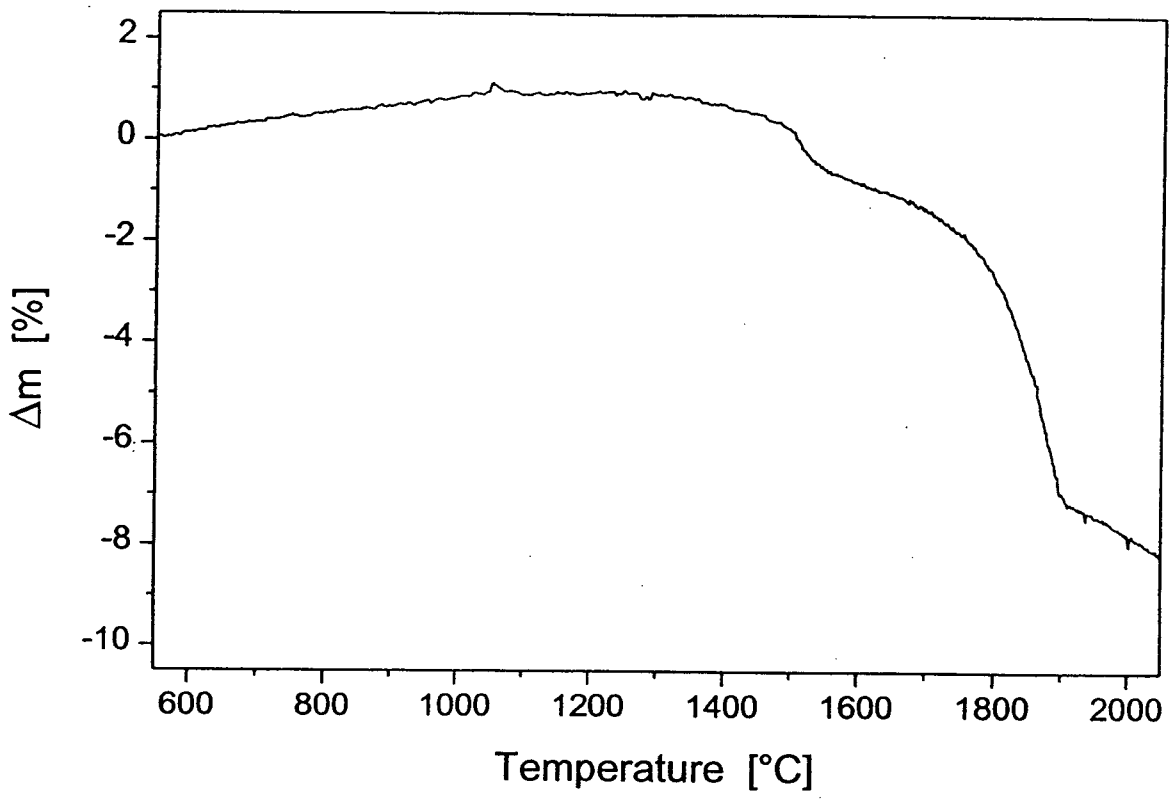
2
0
-2
-4
-6
-8
-10
Δm [%]
600
800
1000
1200
1400
1600
1800
2000
Temperature [°C]

Figure 3.

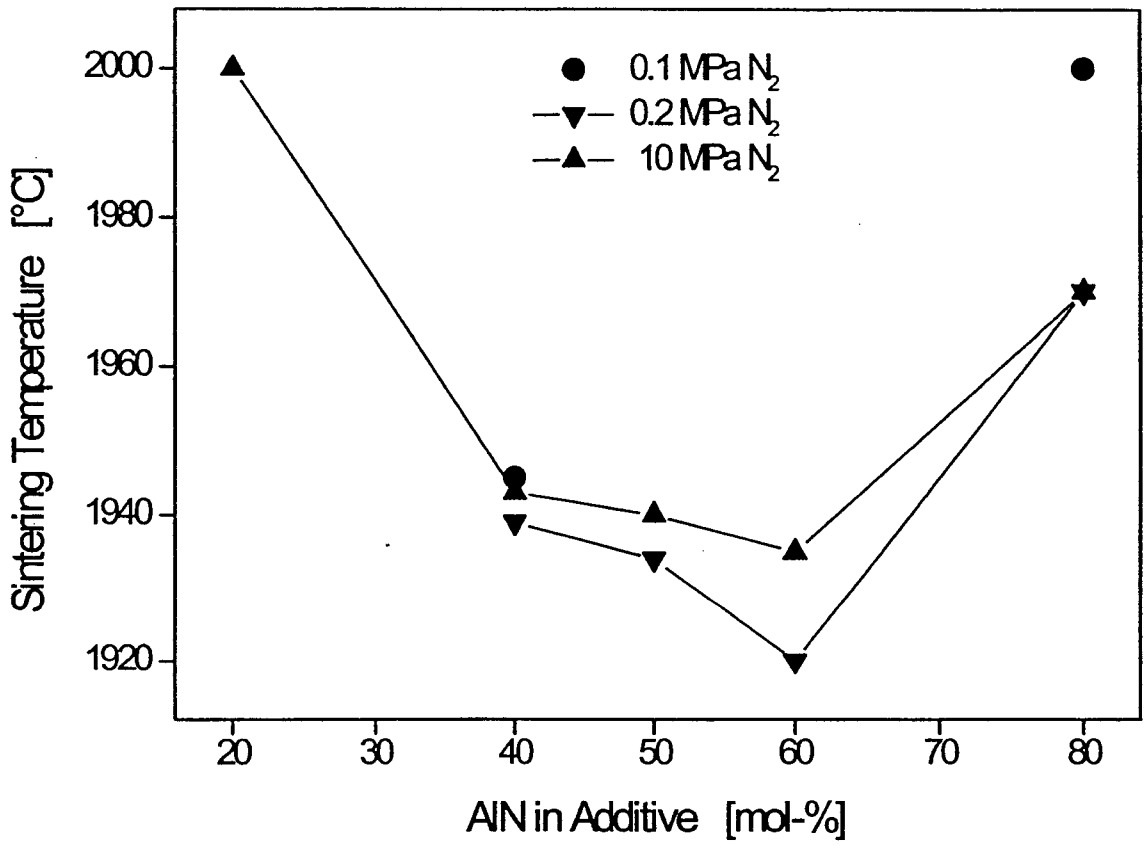
0.1 MPa N2
0.2 MPa N2
10 MPa N2
Sintering Temperature [°C]
2000
1980
1960
1940
1920
20
30
40
50
60
70
80
AlN in Additive [mol-%]

Figure 4.

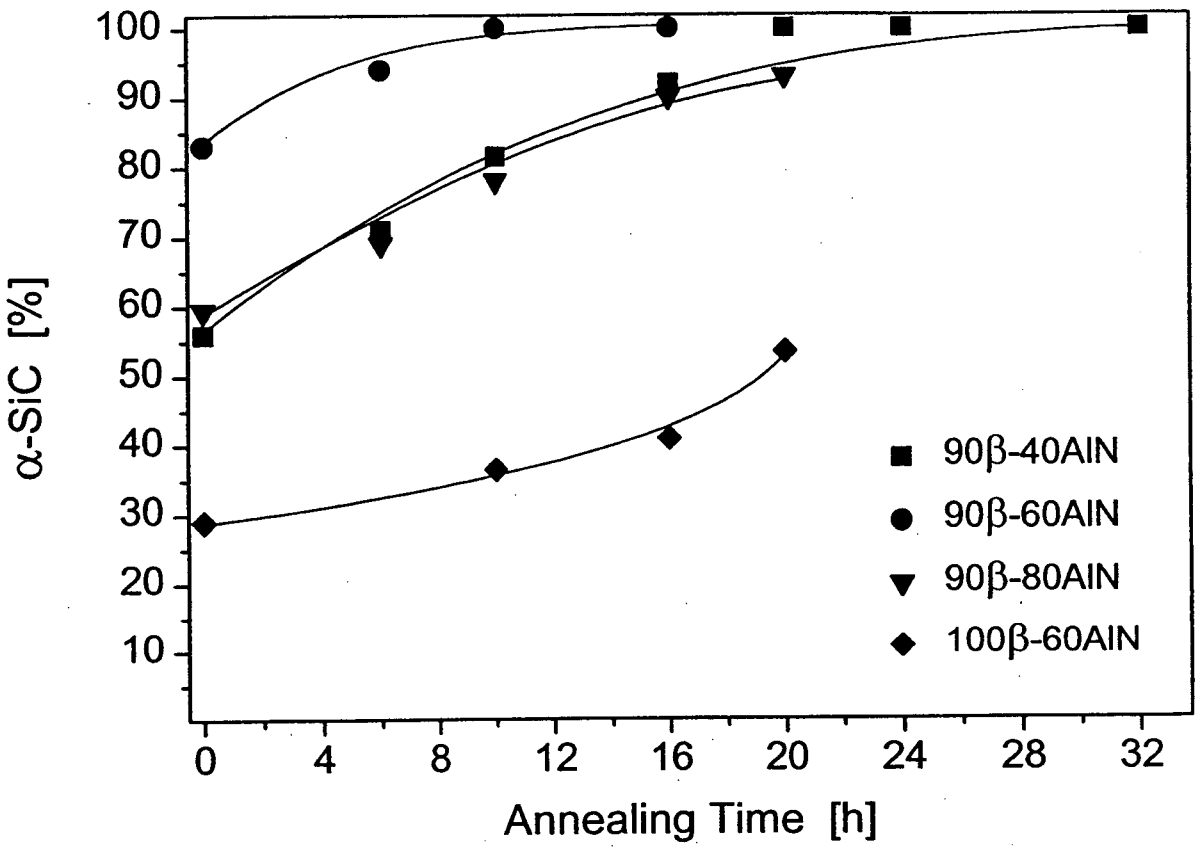
α-SiC [%]
100
90
80
70
60
50
40
30
20
10
0
4
8
12
16
20
24
28
32
Annealing Time [h]
90β-40AlN
90β-60AlN
90β-80AlN
100β-60AlN

Figure 5.

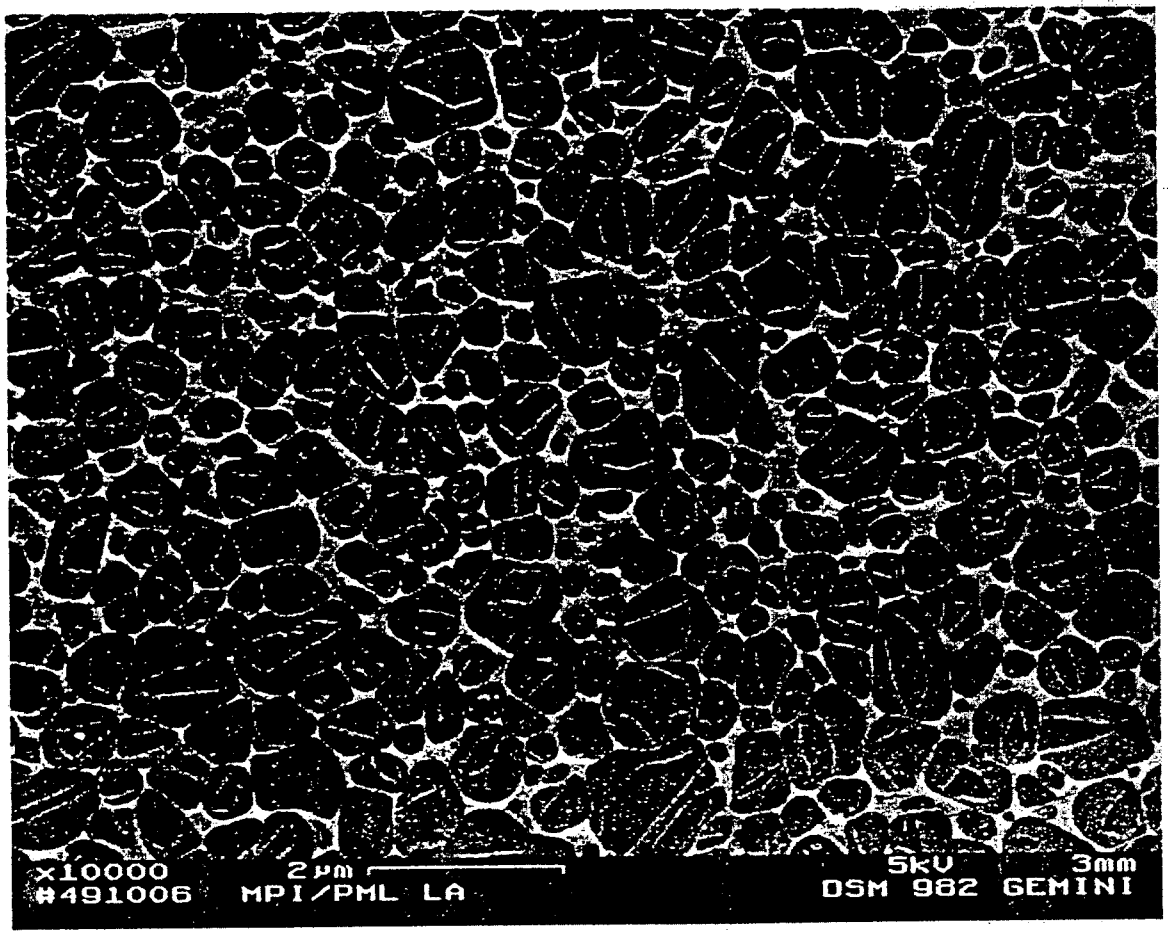

Figure 6 (a).

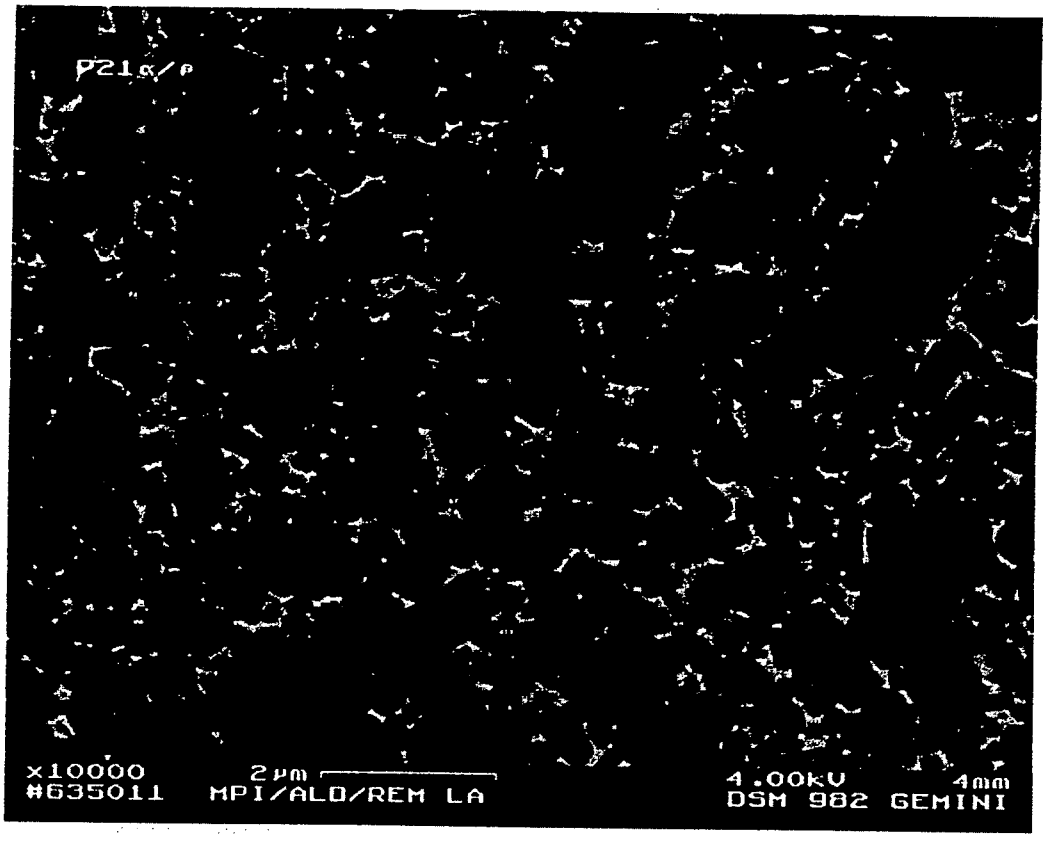
P21α/P
x10000
#635011
2μm
MPI/ALD/REM LA
4.00kV
4mm
DSM 982 GEMINI

Figure 6 (b).

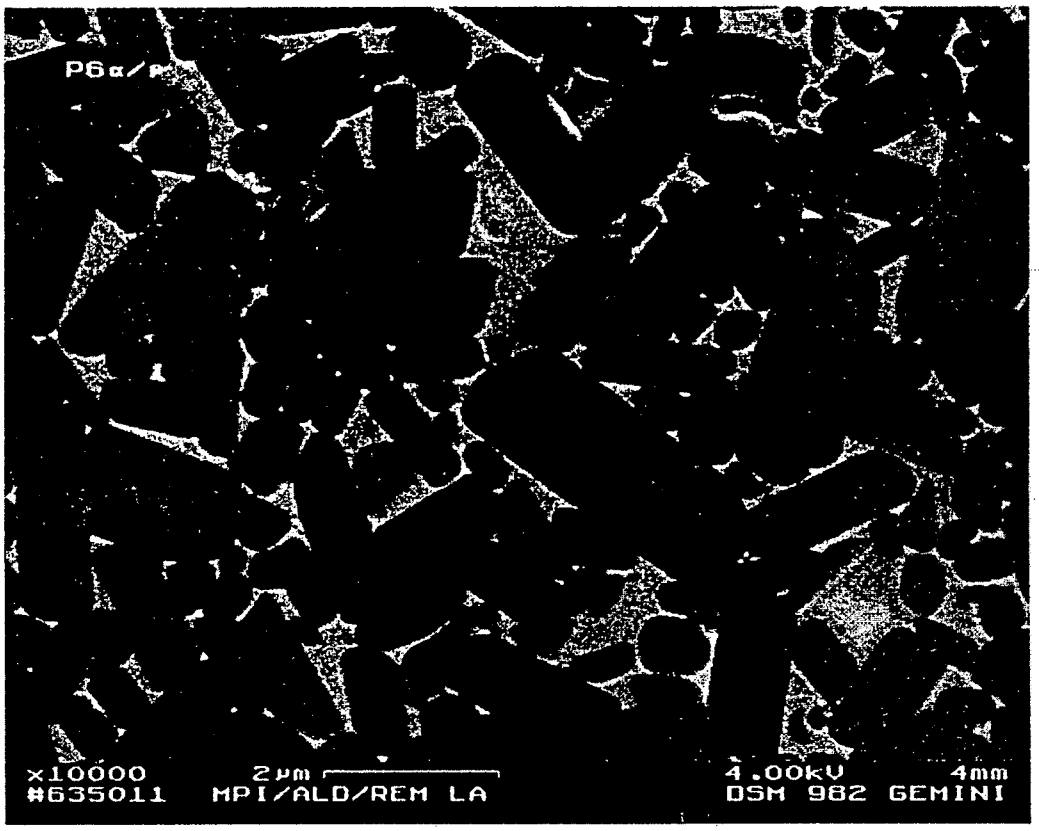
P6α/P
x10000
#635011
2μm
MPI/ALD/REM LA
4.00kV
4mm
DSM 982 GEMINI

Figure 6 (c).

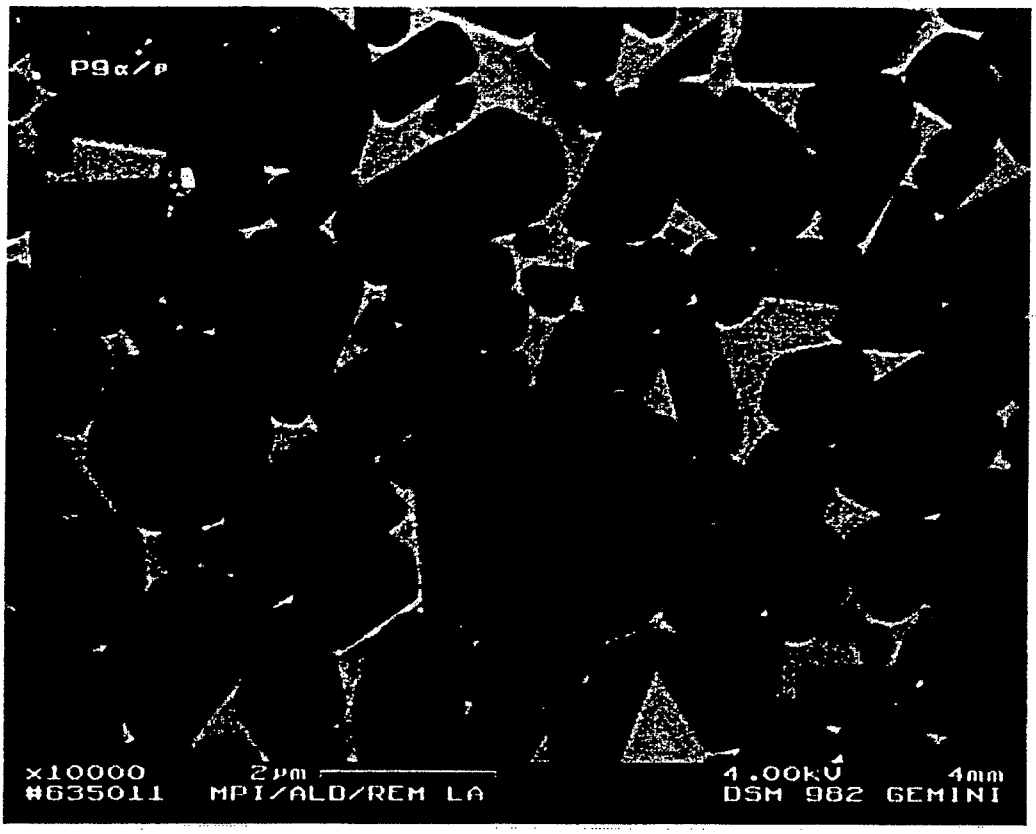

Figure 7 (a).

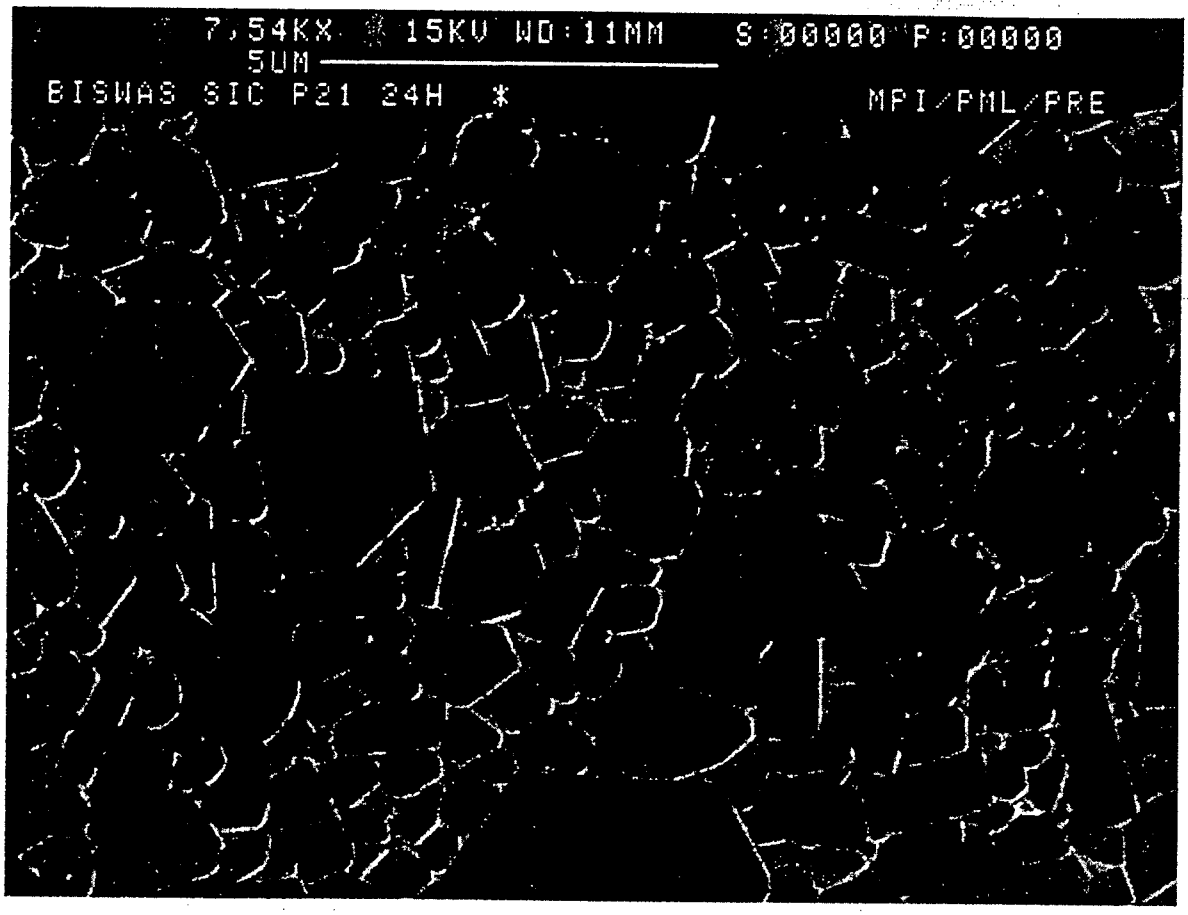
7.54KX 15KV WD:11MM S:00000 P:00000
SUM
BISWAS SIC P21 24H *
MPI/PML/PRE

Figure 7 (b).

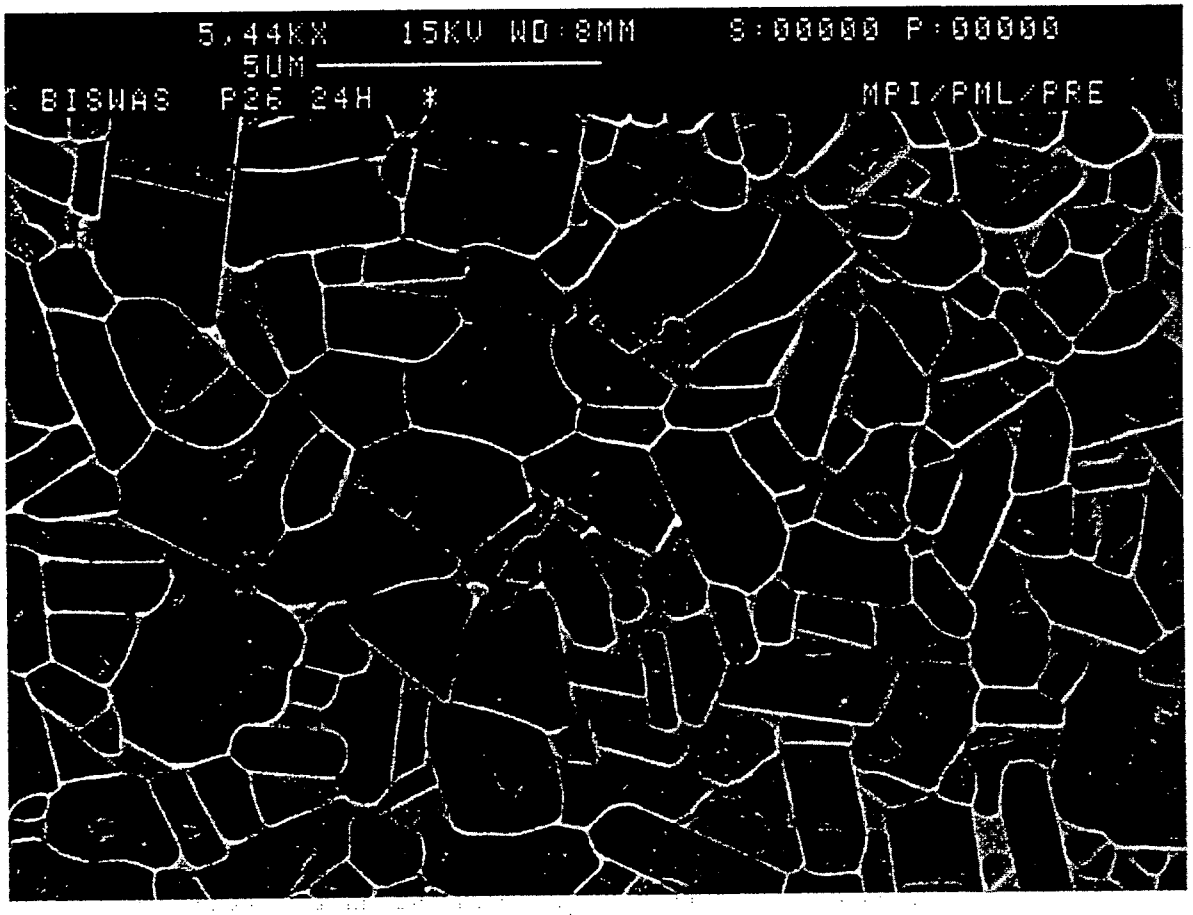
5.44KX 15KV WD:8MM S:00000 P:00000
5UM
BISWAS P26 24H *
MPI/PML/PRE

Figure 8.

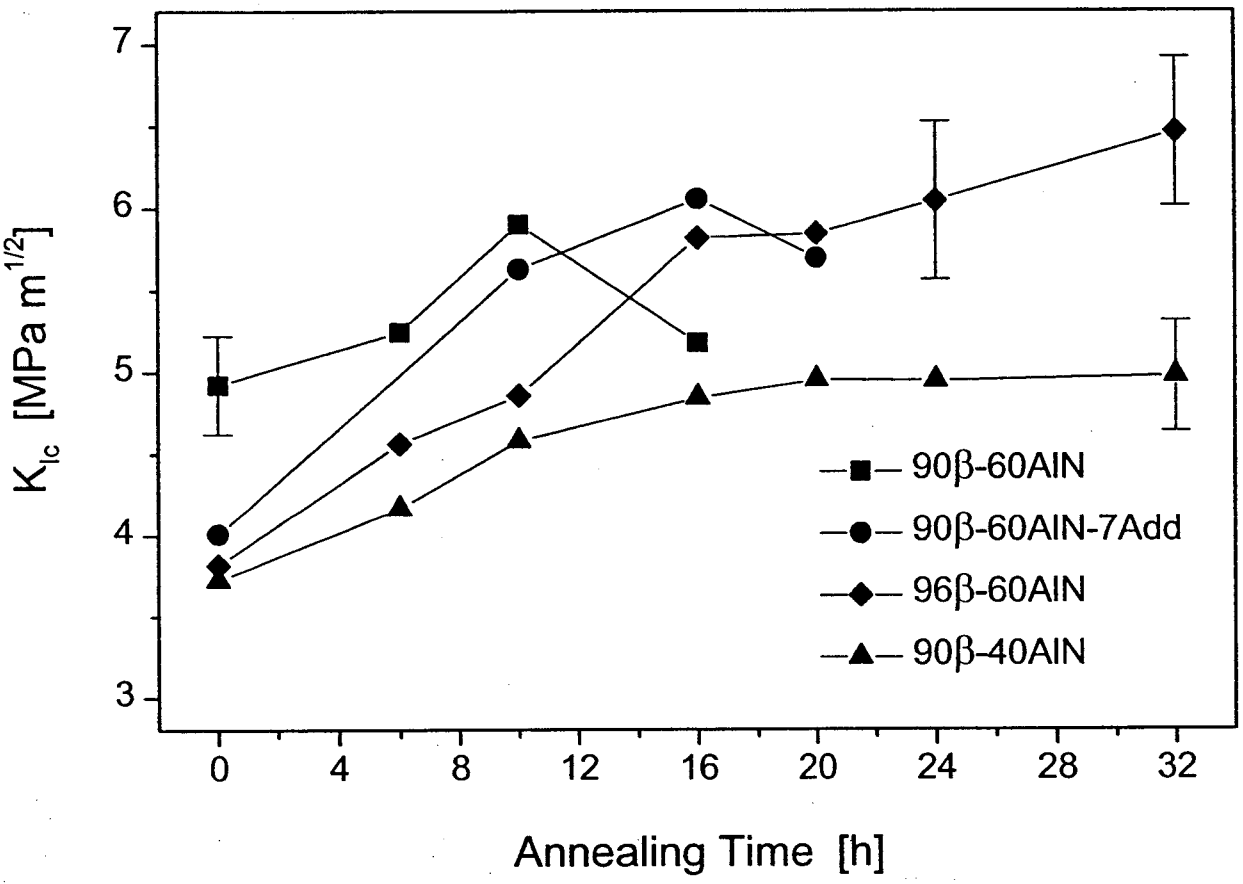
7
6
5
4
3
K_{Ic} [MPa $m^{1/2}$]
0
4
8
12
16
20
24
28
32
Annealing Time [h]
90β-60AlN
90β-60AlN-7Add
96β-60AlN
90β-40AlN

Figure 9.

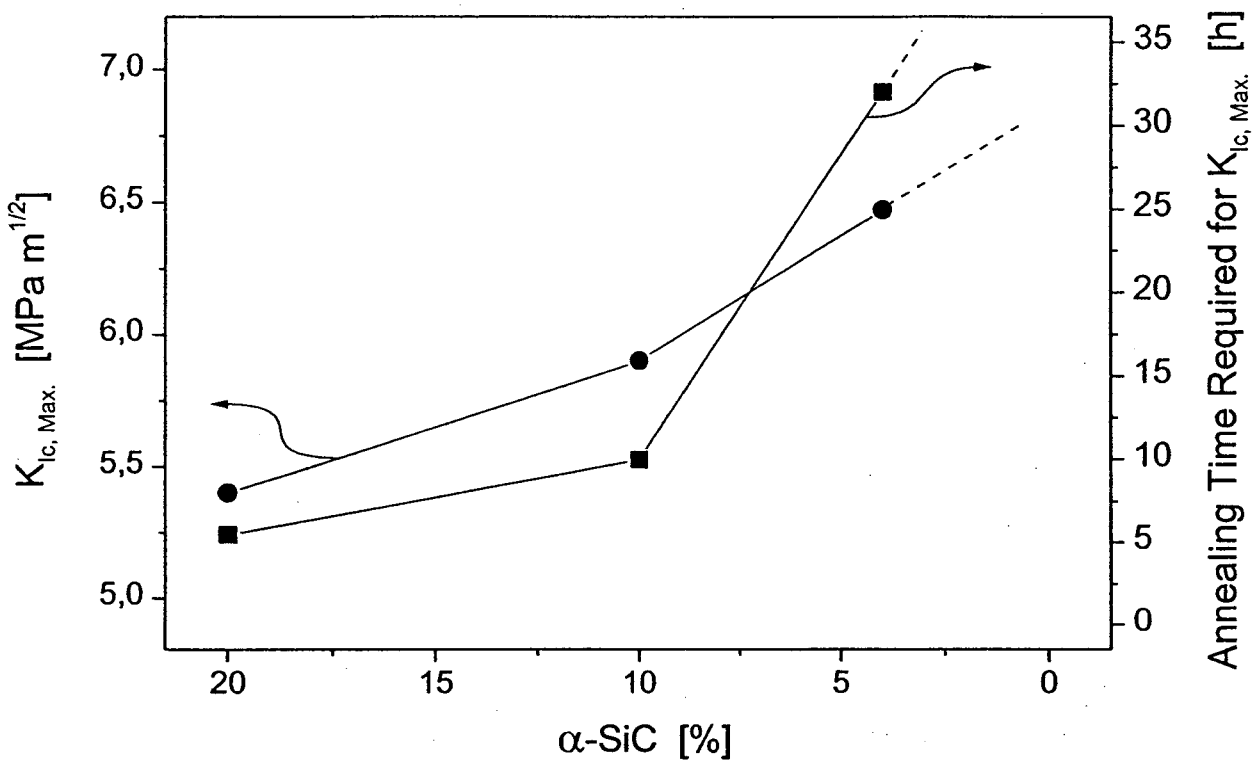
7,0
6,5
6,0
5,5
5,0
$K_{Ic, Max.}$ [MPa $m^{1/2}$]
20
15
10
5
0
α-SiC [%]
35
30
25
20
15
10
5
0
Annealing Time Required for $K_{Ic, Max.}$ [h]

Figure 10.

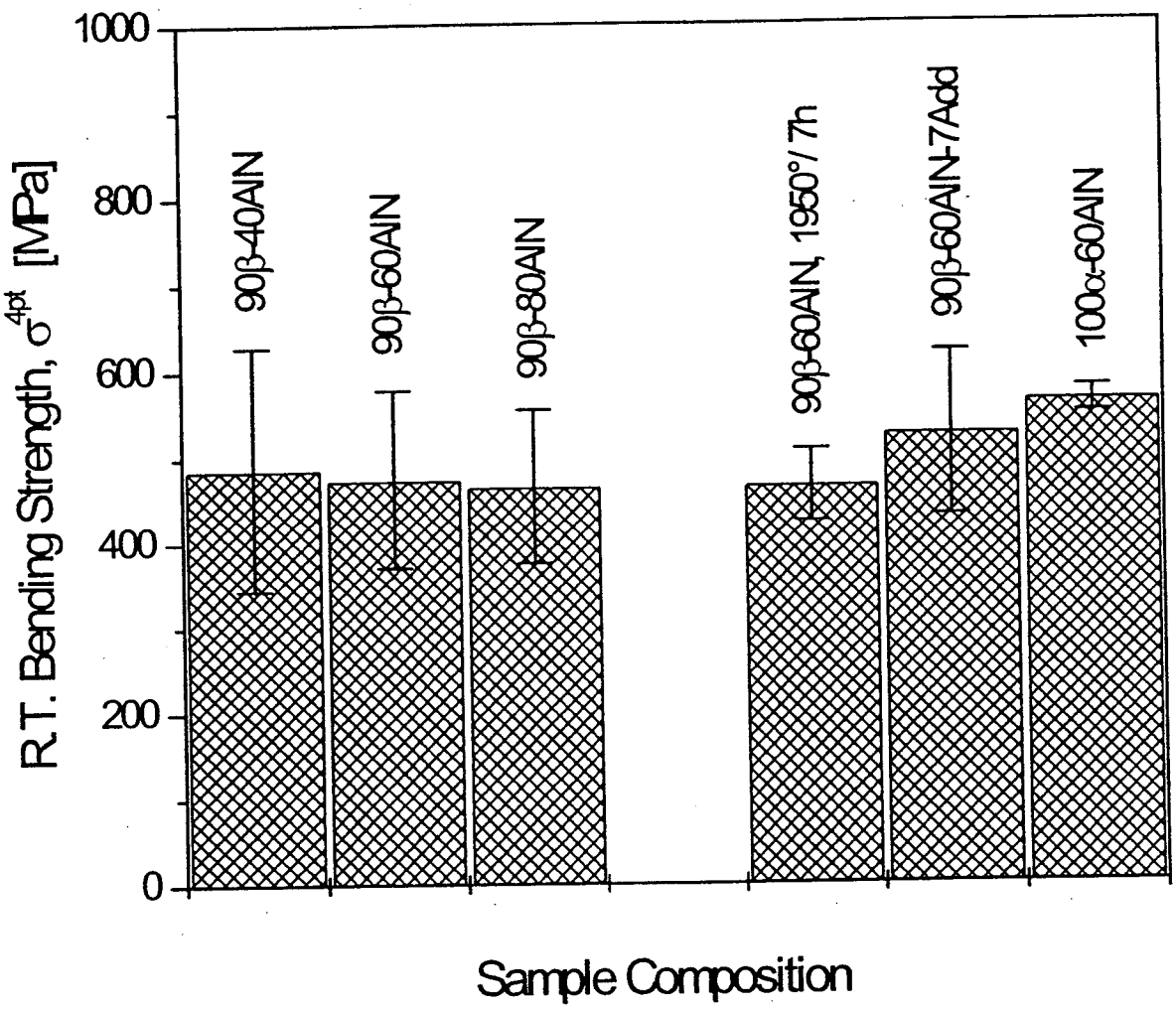
R.T. Bending Strength, σ^{4pt} [MPa]
1000
800
600
400
200
0
90β-40AlN
90β-60AlN
90β-80AlN
90β-60AlN, 1950°/ 7h
90β-60AlN-7Add
100α-60AlN
Sample Composition

Figure 11.

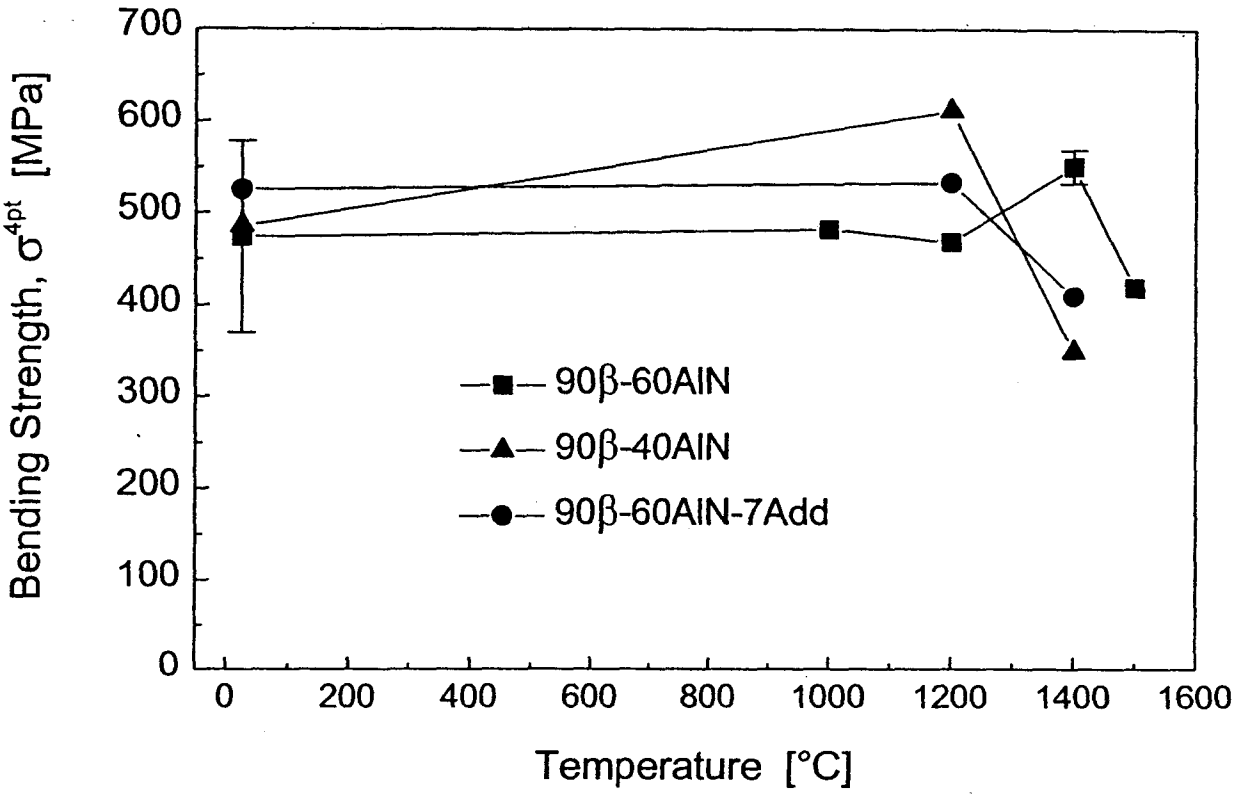
Bending Strength, σ4pt [MPa]
700
600
500
400
300
200
100
0
0
200
400
600
800
1000
1200
1400
1600
Temperature [°C]
90β-60AlN
90β-40AlN
90β-60AlN-7Add

Figure 12.

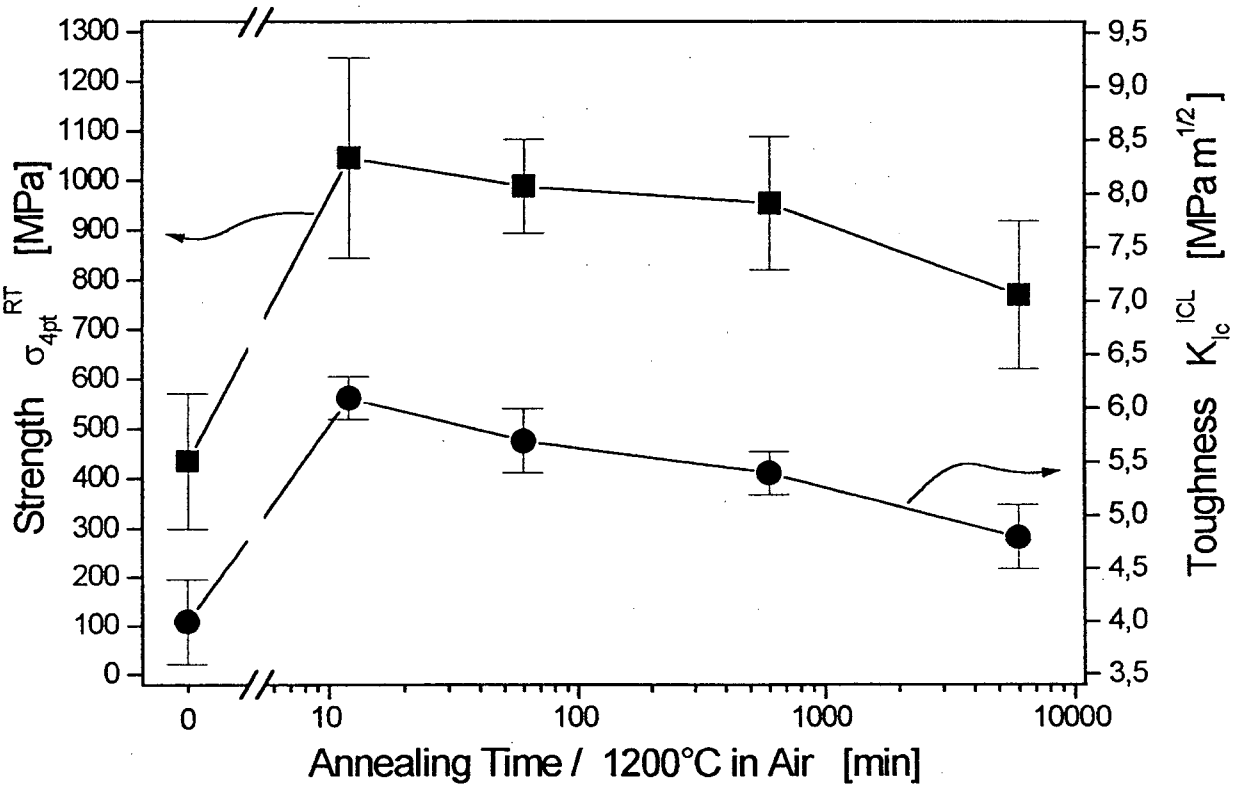
Strength σ_{4pt}^{RT} [MPa]
Toughness K_{Ic}^{ICL} [MPa m$^{1/2}$]
Annealing Time / 1200°C in Air [min]
1300
1200
1100
1000
900
800
700
600
500
400
300
200
100
0
9,5
9,0
8,5
8,0
7,5
7,0
6,5
6,0
5,5
5,0
4,5
4,0
3,5
0
10
100
1000
10000